

Article

Photodegradation of Wastewater Containing Organic Dyes Using Modified G-C₃N₄-Doped ZrO₂ Nanostructures: Towards Safe Water for Human Beings

Ahmed T. Mosleh^{1,2,3} , Fatemah F. Al-Harbi⁴, Soumaya M. Gouadria⁴, Samer H. Zyoud^{5,6,7,*} , Heba Y. Zahran⁸ , Mai S. A. Hussien^{1,2} and Ibrahim S. Yahia⁸ 

- ¹ Department of Chemistry, Faculty of Education, Ain Shams University, Roxy, Cairo 11757, Egypt
² Nanoscience Laboratory for Environmental and Bio-Medical Applications (NLEBA), Green Research Laboratory (GRL), Faculty of Education, Ain Shams University, Roxy, Cairo 11757, Egypt
³ Nanotechnology Section, Egyptian Company for Carbon Materials, El-Sheraton/El-Nozha, Cairo 11757, Egypt
⁴ Department of Physics, College of Science, Princess Nourah bint Abdulrahman University, P.O. Box 84428, Riyadh 11671, Saudi Arabia
⁵ Department of Mathematics and Sciences, Ajman University, Ajman P.O. Box 346, United Arab Emirates
⁶ Center of Medical and Bio-Allied Health Sciences Research (CMBHSR), Ajman University, Ajman P.O. Box 346, United Arab Emirates
⁷ Nonlinear Dynamics Research Center (NDRC), Ajman University, Ajman P.O. Box 346, United Arab Emirates
⁸ Laboratory of Nano-Smart Materials for Science and Technology (LNSMST), Department of Physics, Faculty of Science, King Khalid University, P.O. Box 9004, Abha 61413, Saudi Arabia
* Correspondence: s.zyoud@ajman.ac.ae; Tel.: +971-507771228



Citation: Mosleh, A.T.; Al-Harbi, F.F.; Gouadria, S.M.; Zyoud, S.H.; Zahran, H.Y.; Hussien, M.S.A.; Yahia, I.S. Photodegradation of Wastewater Containing Organic Dyes Using Modified G-C₃N₄-Doped ZrO₂ Nanostructures: Towards Safe Water for Human Beings. *Catalysts* **2024**, *14*, 42. <https://doi.org/10.3390/catal14010042>

Academic Editors: Tamara B. Ivetić, Biljana F. Abramovic and Hideyuki Katsumata

Received: 1 November 2023

Revised: 30 November 2023

Accepted: 15 December 2023

Published: 7 January 2024



Copyright: © 2024 by the authors. Licensee MDPI, Basel, Switzerland. This article is an open access article distributed under the terms and conditions of the Creative Commons Attribution (CC BY) license (<https://creativecommons.org/licenses/by/4.0/>).

Abstract: Historically, the photocatalytic efficacy of graphitic carbon nitride (g-C₃N₄) has been constrained by a rapid charge recombination rate and restricted sensitivity to visible light. To overcome these limitations and enhance the performance of g-C₃N₄, the strategic formation of heterojunctions with semiconductor materials is deemed the optimal approach. The present study employed a facile sonication-assisted pyrolysis method to synthesize a g-C₃N₄@ZrO₂ nanocomposite photocatalyst. This hybrid material was characterized extensively using a comprehensive suite of analytical techniques, including XRD, SEM, EDX, FTIR, and UV-Vis DRS. A comparative analysis of photocatalytic applications under identical conditions was conducted for all synthesized materials, wherein they were subjected to UVc light irradiation. The photocatalytic degradation of various dye models, such as MB, EY, and a combination of dyes, was assessed using the prepared nanocomposites. The g-C₃N₄@ZrO₂ photocatalysts showcased superior photocatalytic performance, with a particular variant, g-CNZ₆, exhibiting remarkable activity. With a bandgap energy of 2.57 eV, g-CNZ₆ achieved impressive degradation efficiencies of 96.5% for MB and 95.6% for EY within 40 min. Following previous studies, the superoxide radical anions (O₂^{•-} and h⁺) were largely accountable for the degradation of MB. Therefore, the observed efficacy of the g-C₃N₄@ZrO₂ nanocomposite photocatalyst can be attributed to the increased generation of these reactive species.

Keywords: photocatalyst; Methylene Blue; Eosin Yellow; thermal polycondensation; g-C₃N₄@ZrO₂; EDX-FTIR-XRD-SEM

1. Introduction

Human history has been marked by an escalating stress on natural resources, with the past century seeing the most acute increase, principally due to the dramatic surge in the population and the significant demand to feed and sustain such a populace [1]. Numerous global challenges have come to the fore, including mounting demands for, and the scarcity of, freshwater sources, a crisis precipitated by rampant industrialization, a burgeoning population, and relentless aridity [2]. Imperative to environmental preservation is removing hazardous dyes from the wastewater discharge of the industries of textiles and pharmaceuticals [3].

Many water purification techniques have been utilized to cleanse contaminated water, notably reverse osmosis, sedimentation, electrochemical fragmentation, ion exchange, chlorination, and photocatalysis [4–6]. Among these, the photocatalytic degradation of harmful pollutants is gaining prominence due to its unique attributes, such as using renewable energy, environmental benignity, and superior efficacy compared to conventional methodologies [7,8]. Solar photocatalysis, which leverages high-efficiency photocatalysts, semiconductor materials, and abundant solar energy, is increasingly recognized by the scientific community as a promising eco-energetic solution [9–15].

Within materials science, two-dimensional layered materials of graphitic carbon nitride ($g\text{-C}_3\text{N}_4$) have become a focal point due to their semi-conductor nature, manageable energy gap, cost-effectiveness, ease of preparation, high chemical stability, non-polluting feature, and abundant active sites, thereby functioning as an effective metal-free and visible light-responsive photocatalyst [16,17]. $g\text{-C}_3\text{N}_4$, distinguished by its low direct band gap (2.7 eV), has garnered attention for its superior attributes like excellent visible light absorption (>460 nm), remarkable photochemical capabilities, and exceptional thermal and chemical resilience [18,19]. $g\text{-C}_3\text{N}_4$'s structure parallels that of graphite but with layers held together by van der Waals forces and each layer possessing robust covalent C–N bonds instead of C–C bonds. It exhibits substantial stability against thermal and chemical attacks, owing to its “poly (tri-s-triazine)” structure and a high degree of condensation [20].

However, pure $g\text{-C}_3\text{N}_4$'s photocatalytic efficacy is typically limited due to its restricted solar light absorption, small surface area, and short-lived photogenerated electron–hole pairs [21]. As a result, several enhancement strategies have been pursued, including molecular and elemental doping, fabrication, exfoliation to create two-dimensional (2D) nanosheets, combination with conductive materials, nanocomposite structures, and heterojunction creation [2,22–25].

Heterojunction creation has emerged as an optimal method to enhance $g\text{-C}_3\text{N}_4$'s efficiency. Several heterojunction types exist, classified by the relative positions of the band gaps, including type-I, type-II, p-n, S-scheme, and Z-scheme heterojunctions [26–28]. A unique electron transport mechanism enables the congregation of photogenerated electrons and holes in a direct Z-scheme system within the conduction band (CB) with a higher reduction potential and the valence band (VB) with a greater oxidation potential, respectively [29,30]. Due to the electrostatic interactions, it is easier for photogenerated electrons to migrate from component II's CB to component I's hole-rich VB [31]. $g\text{-C}_3\text{N}_4$ nanosheets are an excellent choice for creating Z-scheme heterojunctions due to their notable stability, substantial surface area, and fitting band level with ZrO_2 [32].

ZrO_2 , an n-type semiconductor metal oxide, has attracted significant attention due to its desirable attributes such as excellent optical properties, high thermal stability, non-toxicity, oxidation and reduction resistance, and cost-effectiveness [33–35]. However, the wide band gap of ZrO_2 (around 5.1 eV) restricts its ability to absorb UV–visible light, which comprises about 4% of the solar spectrum, limiting its use in real-world applications. The low separation rate of photogenerated carriers within ZrO_2 also inhibits its photocatalytic activity [36,37]. Combining $g\text{-C}_3\text{N}_4$ and nano-structured ZrO_2 can improve charge carrier separation and increase specific surface area, rendering $g\text{-C}_3\text{N}_4@ZrO_2$ a potentially effective photocatalyst.

Methylene Blue (MB) is a widely used cationic dye in industries concerning printing, pharmaceuticals, cosmetics, and textiles, but it can cause skin irritation, allergic dermatitis, cancer, and genetic mutations [38]. Eosin Yellow (EY), an anionic xanthene dye, is frequently used in producing ink, textiles, and pharmaceutical products. Its effluents, however, can inhibit protein interactions, irritate the skin, and cause genotoxicity in humans, necessitating its detoxification [39,40]. The synthesized $g\text{-C}_3\text{N}_4@ZrO_2$ photocatalysts have demonstrated excellent photocatalytic activity for the degradation of MB and EY dyes.

This study utilized thermal combustion to synthesize $g\text{-C}_3\text{N}_4@ZrO_2$ nanocomposite photocatalysts easily. XRD, SEM, EDX, FTIR, and UV–Vis DRS characterized all the produced nanocomposites. Our findings unveiled how the ZrO_2 mass influenced the

morphology and crystal structure of the $g\text{-C}_3\text{N}_4@\text{ZrO}_2$ nanocomposite and how this subsequently affected the activity and selectivity of the photodegradation of MB, EY, and mixed dye under UV light illuminations.

2. Results and Discussion

2.1. XRD Analysis

X-ray diffraction (XRD) analysis is a crucial technique in inspecting the heterojunctions and phase structures of pristine materials. Illustrated in Figure 1 are the XRD spectra obtained from the $g\text{-CN}$ nanosheet samples. This layer contains an aromatic component, sp^2 , displaying a hybridized three-s-triazine structure [41]. Concurrently, the (002) planes of the graphitic carbon nitride phase of the hexagonal crystal for [JCPDS 87-1526] resulted in two diffraction peaks, specifically at 12.8° and 27.3° for $g\text{-CN}$ [42].

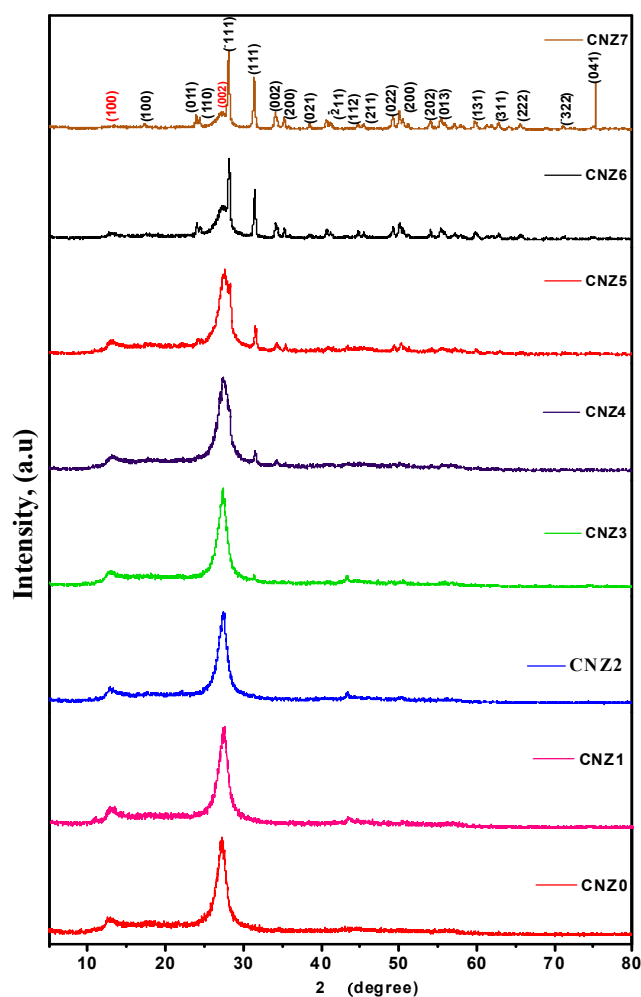


Figure 1. X-ray diffraction patterns of $g\text{-CN}$ and $g\text{-CNZ}$ nanostructured samples.

Notably, the (002) diffraction peak appears relatively weaker for the synthesized $g\text{-CN}$ nanosheet and particle. This observation considers the surface area ratio between two distinct peaks and suggests a decrease in the layered structural elements. The diffraction peak of the (002) plane in the $g\text{-CN}$ nanosheet undergoes a slight shift from 27.3° to 28.1° , signifying the thermal exfoliation of the $g\text{-CN}$ [43].

Figure 1 displays the XRD diffraction peaks of ZrO_2 with varied morphologies. According to the findings (JCPDS 01-078-0047), the produced ZrO_2 exhibits monoclinic phases. Diffraction peaks occur at 2θ : 17.28° , 23.96° , 24.42° , 28.15° , 31.4° , 34.16° , 35.30° , 38.52° , 44.82° , 49.22° , 50° , 54.02° , 55.34° , 59.76° , 62.82° , 65.68° , 71.06° , and 75.20° , corresponding to the monoclinic phase, and which are conveniently assigned to the planes of (100), (011),

(110), (−111), (111), (002), (200), (021), (−211), (112), (211), (022), (200), (202), (013), (131), (311), (222), (−322), and (041) [44,45] respectively. It has also been found, in Figure 1, that the g-CN diffraction peaks rise while the ZrO₂ content decreases in the synthesized samples.

To determine the average crystallite size, lattice strain, and dislocation density of the samples, Debye–Scherrer’s formula was applied [46]:

$$D = \frac{k \lambda}{\beta \cos\theta} \quad (1)$$

where D is the size of the crystallite, β is the full width at half maximum (FWHM), λ is the wavelength, and lattice strain (ε) was determined [46]:

$$\varepsilon = \frac{\beta \cos\theta}{4} \quad (2)$$

while dislocation density (δ) was obtained through the following:

$$\delta = \frac{1}{D^2} \quad (3)$$

Table 1 lists the average crystallite size values derived, the lattice strain determined from the XRD spectra, and the dislocation for all the manufactured samples. Additionally, the FWHM is β , and the diffraction peak angle is θ , respectively. The lattice strain, dislocation, and average crystallite size values computed using the XRD spectra for the first phase was determined to be between 10.011 and 17.029 nm, whereas the average crystallite size for the ZrO₂ phase was between 7.422 and 33.167 nm. It should be observed that the size of the crystallites tends to grow as the strain decreases. Equation (4) demonstrates that the lattice strain value relies on both β and $\cos\theta$, and are given in Table 1, together with the mean values of the lattice strain for each phase obtained. The range of the g-C₃N₄ phase’s lattice strain means was 2.683×10^{-3} to 3.456×10^{-3} . At the same time, for the ZrO₂ phase, this varied from 1.84×10^{-3} to 4.670×10^{-4} . As stated in Equation (5), the dislocation density (δ) can also be used to determine crystallinity. The g-C₃N₄ phase varied between 6.511 and 10.615×10^{-3} and between 1.045 and 8.816×10^{-3} for the ZrO₂ phase. It was indicating that linked ZrO₂ levels were rising. The XRD data generally supported the creation of the gC₃N₄@ZrO₂ heterojunction photocatalyst using the one-pot synthesis method.

Table 1. The computed mean values of the crystallite size, dislocation density, and strain from the XRD spectra for CN and CNZ NCs samples.

Samples	Phases	Crystallite Size (nm)	Dislocation (δ) (nm) ²	Lattice Strain
CNZ ₀	Phase 1, C ₃ N ₄	10.678	9.769×10^{-3}	3.366×10^{-3}
CNZ ₁	Phase 1, C ₃ N ₄	10.687	9.769×10^{-3}	3.366×10^{-3}
	Phase 2, ZrO ₂	7.422	1.815×10^{-3}	4.670×10^{-3}
CNZ ₂	Phase 1, C ₃ N ₄	17.029	7.438×10^{-3}	2.683×10^{-3}
	Phase 2, ZrO ₂	16.678	3.675×10^{-3}	2.094×10^{-3}
CNZ ₃	Phase 1, C ₃ N ₄	10.727	9.939×10^{-3}	3.381×10^{-3}
	Phase 2, ZrO ₂	11.793	8.816×10^{-3}	3.151×10^{-3}
CNZ ₄	Phase 1, C ₃ N ₄	14.627	8.128×10^{-3}	2.880×10^{-3}
	Phase 2, ZrO ₂	15.709	5.554×10^{-3}	2.439×10^{-3}
CNZ ₅	Phase 1, C ₃ N ₄	10.011	10.615×10^{-3}	3.456×10^{-3}
	Phase 2, ZrO ₂	19.147	2.997×10^{-3}	1.872×10^{-3}
CNZ ₆	Phase 1, C ₃ N ₄	13.737	6.511×10^{-3}	2.706×10^{-3}
	Phase 2, ZrO ₂	21.197	2.889×10^{-3}	1.782×10^{-3}
CNZ ₇	Phase 1, C ₃ N ₄	12.890	8.637×10^{-3}	3.047×10^{-3}
	Phase 2, ZrO ₂	34.167	1.045×10^{-3}	1.084×10^{-3}

2.2. Morphological Analysis

The scanning electron microscopy (SEM) analysis was meticulously conducted on the g-CN and g-CNZ nanocomposite samples to discern the surface topography and underlying microstructure. Figure 2a distinctly illustrates the lamellar framework and multiplex aggregation phenomena characteristic of pure g-CN [47]. The strikingly divergent morphologies of the two materials are readily distinguishable under the lens of the scanning electron microscope, facilitating differentiation. Accumulated research has postulated that this unique structure could potentially provide a wealth of active sites, augment the migration of the resultant carriers, facilitate the optimal catalyst selection process, and stimulate the evolution of a photocatalyst heterojunction [48]. As revealed in Figure 2b–h, the irregular mass is an assembly of ZrO₂ enveloped by a layer of flaky g-C₃N₄, signifying that the two constituents are meticulously compounded. The particulate dimensions fall within a range of 100 to 260 nm. The distinctive morphologies of the ZrO₂ and g-CN enable the straightforward identification of the two semiconductors in the SEM images. It is observable within the composites that the ZrO₂ nanoparticles are enrobed on the g-CN surface, corroborating that the two components are intimately combined [48]. The composite's energy-dispersive X-ray spectroscopy (EDX) findings are shown in Figure 2. The evenly distributed constituents—namely, C, N, Zr, and O—illustrated in Figure 2e'–h', bolster the presence of the dopant and thus corroborate the successful synthesis of the composite. Following aggregation, the photocatalysts' morphologies exhibit a uniform dispersion, indicative of the crystalline ZrO₂'s effect inherent in the composite photocatalyst, a conclusion that aligns with the XRD outcomes [49].

2.3. HRTEM Analysis

Figure 3 shows the TEM images of the g-CNZ₆ nanocomposite. g-C₃N₄ is shown as a nanosheet with its heterojunctions. As observed in Figure 3a, g-C₃N₄ exhibits a large and ultrathin wrinkled nanosheet morphology, which is because of the thermal exfoliation of the CN bulk, and the ZrO₂ irregular spherical nanostructure is deposited on the g-C₃N₄ nanosheet to form g-C₃N₄@ZrO₂ heterojunctions. The particle diameters of 6–8 nm of the ZrO₂ nanostructures in the heterojunction samples are also shown. The surface energy affected by the size and shape of the ZrO₂ nanostructures can be influenced by their amount and distribution over the g-C₃N₄ nanosheet. Close interfacial contact between g-C₃N₄ nanosheet and ZrO₂ nanoparticle is expected to improve the transfer and separation of the excited e[−]_{CB}–h⁺_{VB} pairs and increase the heterojunction photocatalytic performance [48]. Compared with the non-crystalline structure of g-C₃N₄, the g-CNZ nanocomposite displayed crystallinity. The ZrO₂ structure, shown in Figure 3b, with an interplanar spacing of 0.31 nm, was related to the (−111) planes of the ZrO₂ phases, as shown in Figure 3b [49]. In the SAED patterns in Figure 3c, the bright spots confirm the high crystallinity of the sample. The well-resolved crystalline rings in the SAED correspond to the (111) and (−111) planes of the monoclinic zirconia nanoparticles, which match well with the observed XRD patterns. Figure 3d–h shows the mapping of all the elements in the g-CNZ₆ nanocomposite. The photocatalyst confirms that the composite g-CNZ₆ samples contain C, N, Zr, and O elements.

2.4. Functional Group Analysis

Figure 4 delineates the pure g-C₃N₄ and g-C₃N₄@ZrO₂ nanocomposites with their associated FT-IR spectra. Due to the –NH stretching frequencies and incomplete condensation of the NH₂ group, pure g-C₃N₄ distinctly displays a peak within the range of 3500 to 3000 cm^{−1} [32]. The vibrational peaks at 1230, 1323, and 1416 cm^{−1} are attributable to the stretching vibrations of the aromatic C–N, whereas the peak at 1633 cm^{−1} indicates the tensile stretching of the C=N [50,51]. The characteristic triazine structural unit manifests a notable vibrational peak at 807 cm^{−1} [52]. The characteristic ZrO₂ peaks at 715 cm^{−1} are predominantly due to the Zr–O molecular chain vibration [53]. Both the g-C₃N₄ and ZrO₂ distinctive peaks are discernible in the g-C₃N₄@ZrO₂ nanocomposite spectrum, thus

corroborating the successful ZrO₂ incorporation into g-C₃N₄. Additionally, as the quantity of ZrO₂ doping increases, the prominence of the ZrO₂ absorption peak is enhanced, as the XRD data substantiates.

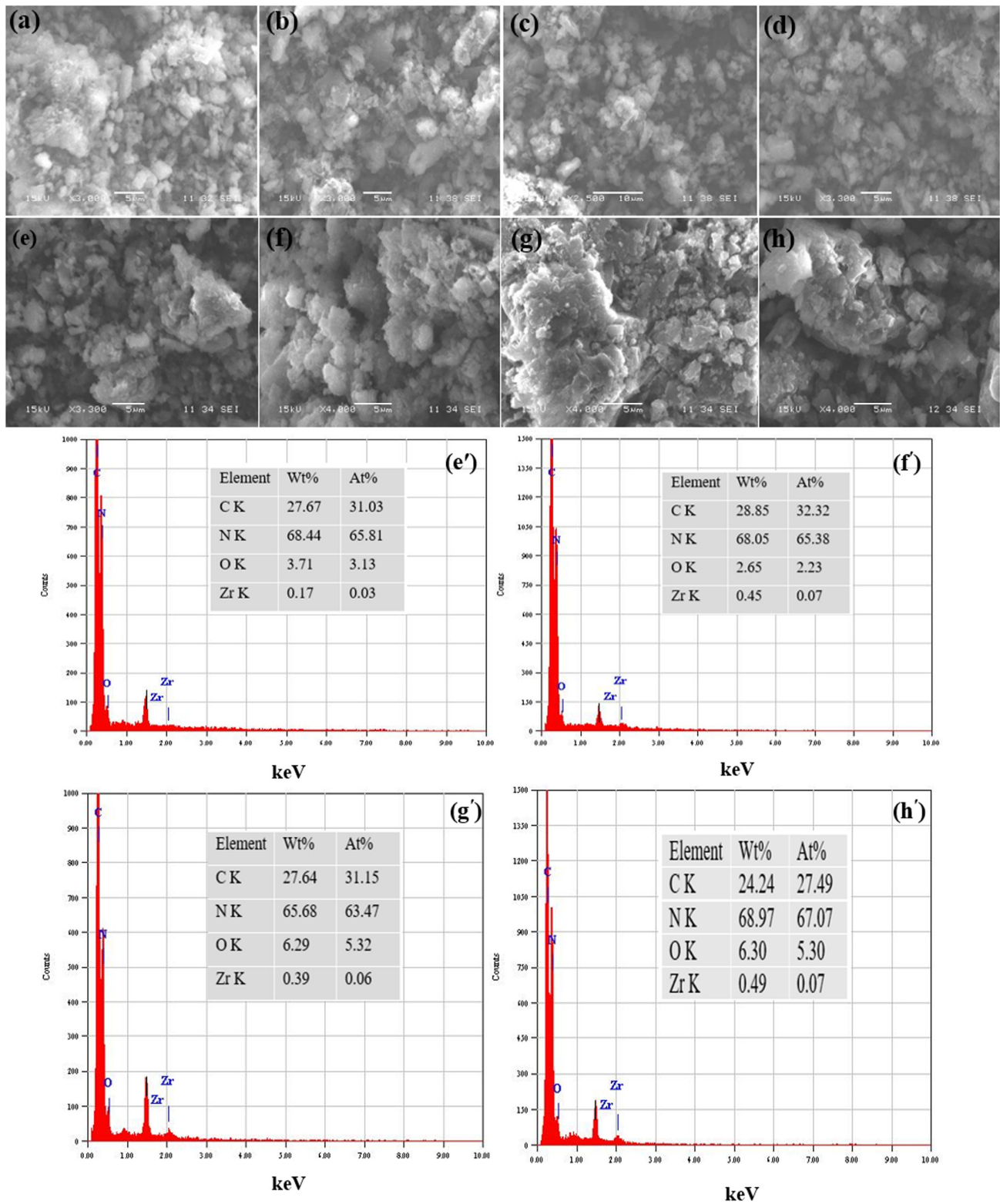


Figure 2. (a–h) SEM images of g-CN and g-CNZ nanocomposite samples, (e'–h') EDX of g-CN₄, g-CN₅, g-CN₆, and g-CN₇ nanocomposite samples.

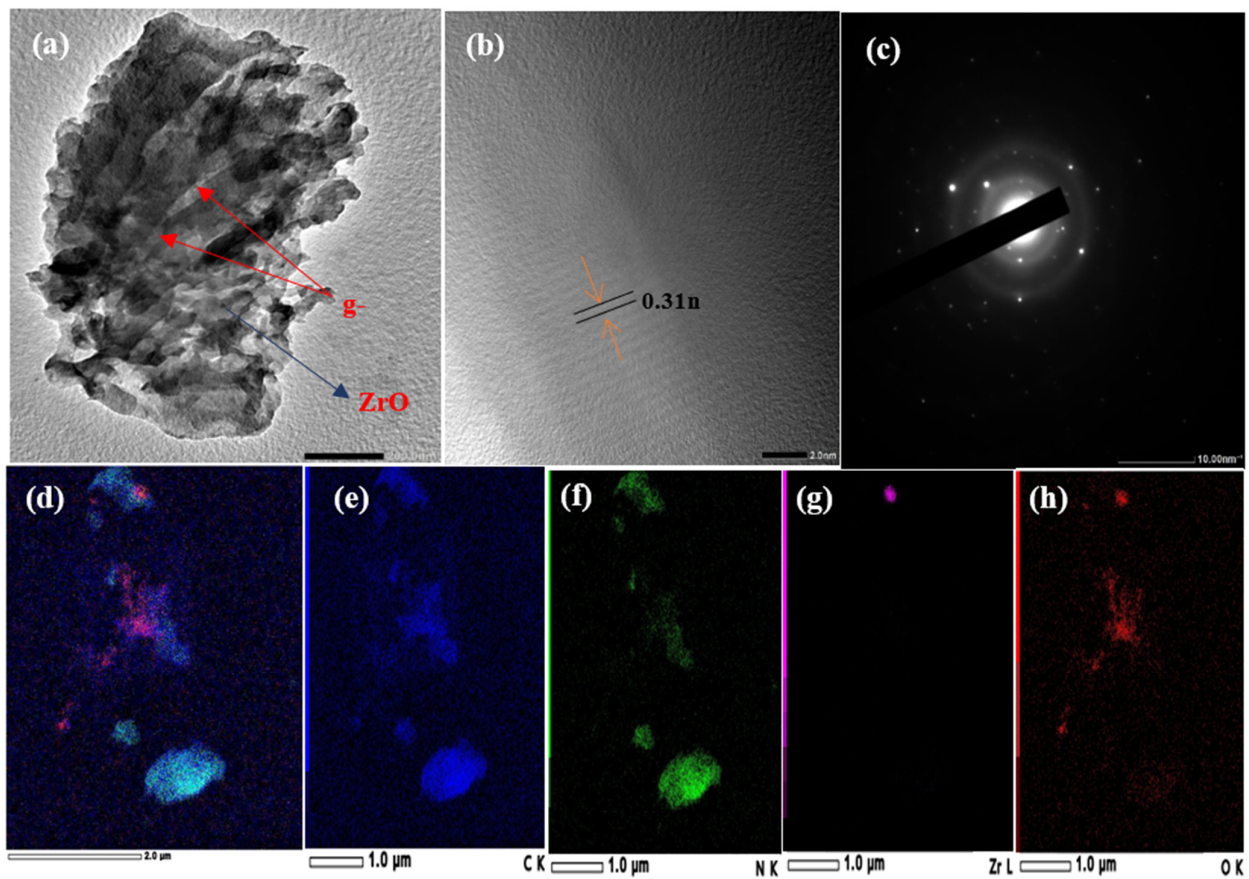


Figure 3. (a) TEM, (b) HRTEM, (c) SAED patterns, and (d–h) elemental mapping of CNZ₆ nanocomposite.

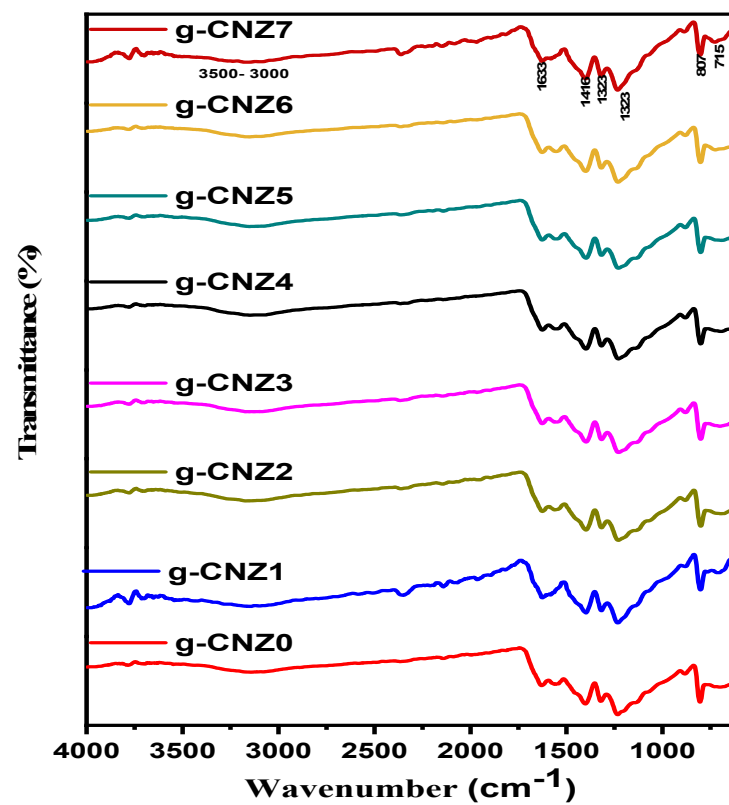


Figure 4. FTIR spectra of g-CN and g-CNZ nanocomposite samples.

2.5. Optical Analysis

Using the UV–Vis diffuse reflectance spectroscopy (DRS) method, the capacity of the photocatalysts to absorb light and generate charge carriers in the g-CN and g-CNZ nanocomposites is assessed. Using the cut line approach, the absorption wavelength threshold is established by creating a tangent and intersection with the abscissa. The raw g-CN absorption edge, visible in Figure 5a, is like that of paper and has a wavelength of about 407 nm. It is located within the visual zone [54]. The percentage reflectance increases with rising ZrO₂ concentrations at extremely low concentrations, peaking for the g-CNZ₃ sample. After that, a definite diminishing trend is seen with increasing ZrO₂ concentrations. The absorption wavelength threshold values for the g-CNZ₃ sample are red-shifted and have a maximum band edge of 388 nm, whereas the pure g-C₃N₄ can absorb light up to a maximum wavelength of 407 nm. The reflectance rises with rising ZrO₂ concentrations at extremely low concentrations, peaking for the g-CNZ₃ sample. After that, an obvious decrease is seen with increasing ZrO₂ concentrations. The highest band edge for the g-CNZ₃ sample is 388 nm, whereas the pure g-C₃N₄ can absorb light up to a maximum wavelength of 407 nm. The values of the absorption wavelength threshold are red-shifted within the range of (388–407 nm). Therefore, adding ZrO₂ makes g-C₃N₄'s ability to absorb visible light more effective. The interaction of ZrO₂ with g-C₃N₄ may lead to chemical bonds being formed between the two semiconductors, improving the optical characteristics and producing charge carriers [55]. From the Tauc's relation provided in the following Equation (6), the calculated band gap E_g of the samples was determined [56]:

$$(\alpha h\nu)^{1/n} = A(h\nu - E_g) \quad (4)$$

where $h\nu$, α , A , and E_g are defined as the incident light frequency, the absorption coefficient, a constant parameter, and the band gap energy, respectively. Also, the value of n depends on the optical transition type in a semiconductor, which is determined to be $\frac{1}{2}$ and 2 for the CNZ₀ and g-CNZ nanocomposites, respectively [56–58]. The n value is $\frac{1}{2}$ for a direct bandgap semiconductor, while for the indirect bandgap materials, the n value will equal 2. The $(\alpha h\nu)^2$ and $(\alpha h\nu)^{1/2}$ vs. $(h\nu)$ graphs were plotted for the direct and indirect bandgap semiconductor, as shown in Figure 5b,c. In the graphs, a straight line is fitted for the straight segment. The straight line to the E axis gives the band gap values. e.g., the values were found to be decreased. The rise in the carrier concentration leads to the development of certain chemical bonds between the g-CNZ₀ and g-CNZ, which is expected to cause a decrease in the band gap and improve the optical characteristics. Table 2 lists all the estimated values for the direct and indirect bandgaps, respectively.

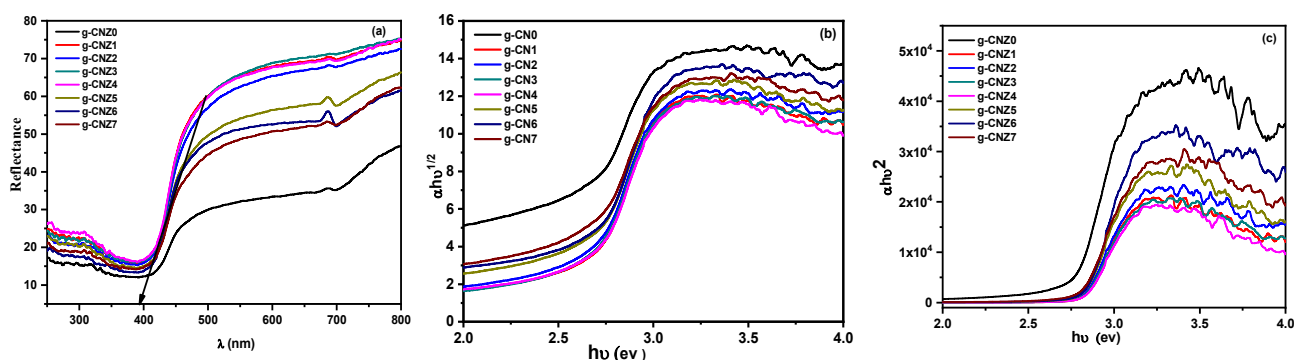


Figure 5. (a) UV–vis DRS spectrum of g-CNZ nanocomposite, (b) direct bandgap, and (c) indirect bandgap.

Table 2. The direct and indirect bandgap of g-CNZ nanocomposites.

Samples	Eg (Indirect)	Eg (Direct)
g-CNZ ₀	2.51	2.61
g-CNZ ₁	2.62	2.81
g-CNZ ₂	2.60	2.80
g-CNZ ₃	2.61	2.81
g-CNZ ₄	2.60	2.79
g-CNZ ₅	2.61	2.79
g-CNZ ₆	2.57	2.78
g-CNZ ₇	2.60	2.80

2.6. Photocatalytic Performance

2.6.1. Photocatalytic Degradation of MB and EY Dyes

Methylene Blue (MB) and eosine yellow (EY), acting as model pollutants, were engaged to evaluate the photocatalytic performance under simulated UVc light irradiation. A thoroughly dark environment was ensured to conduct the adsorption assays of the MB and EY dyes. Approximately half an hour later, a dynamic equilibrium state was achieved, satisfying the stability prerequisites for the adsorption/desorption processes of the tested catalyst specimens.

Figure 6 delineates the absorption intensity recorded at 663 nm, further augmented by the absorption spectra of the MB dye interacting with diverse catalysts throughout the photocatalytic response. Once a photocatalyst is incorporated into the catalytic system, a marked reduction in the MB concentration is observed, which intensifies in direct proportion to the prolonged duration of the catalytic process, as depicted in Figure 6. The efficacy of the MB dye degradation, observed over 40 min of photo-irradiation, is presented in Figure 7a. Table 3 exhibits the perceptible degradation of MB as a consequence of the reaction with the g-CNZ nanocomposites. Following the application of Equation (1), the MB degradation efficiency was determined to be 77.5% and 96.5% for the g-CNZ₀ and g-CNZ₆ nanocomposites, respectively. A substantial enhancement in the photodegradation of the photocatalyst may have been facilitated by the introduction of 0.5 g of ZrO₂ nanoparticles onto the g-CN sheets. This enhancement can be attributed to a robust interfacial interaction, expedited charge mobility, a heightened propensity for charge carrier segregation, and a reduced band gap compared to the g-CNZ₀ and g-CNZ₆ photocatalysts. Photodegradation rate constants, represented by Equation (2) as per [59], were employed to deduce the photodegradation rate constants. The pure g-CNZ₀ displayed a degradation rate of 0.035 min⁻¹. Integrating g-C₃N₄ with ZrO₂ resulted in a remarkable augmentation of the electron–hole separation efficiency and UV light absorption capacity. A concurrent increase in the ZrO₂ compounding quantity led to an escalated degradation rate of 0.088 min⁻¹ for the g-CNZ₆ nanocomposites, thereby outperforming the rate of the pure g-C₃N₄ by a factor of 2.5.

As shown in Figure 8, the absorption spectra of the EY dye with different catalysts during the photocatalytic reaction for the experiment showed an absorption intensity at 520 nm. The EY was used as color pollution, and the photocatalytic performance of the as-prepared catalysts was evaluated. Where deterioration was placed 40 min after photoirradiation, the g-CNZ nanocomposite-enhanced photocatalytic performance is demonstrated by the high degradation efficiency and degradation rate constant (k) values in Table 3. As shown in Figure 9a–c, the degradation efficiency of the g-CNZ₆ nanocomposite within 40 min of light irradiation is up to 95.6%, with a high degradation rate constant (0.0767 min⁻¹).

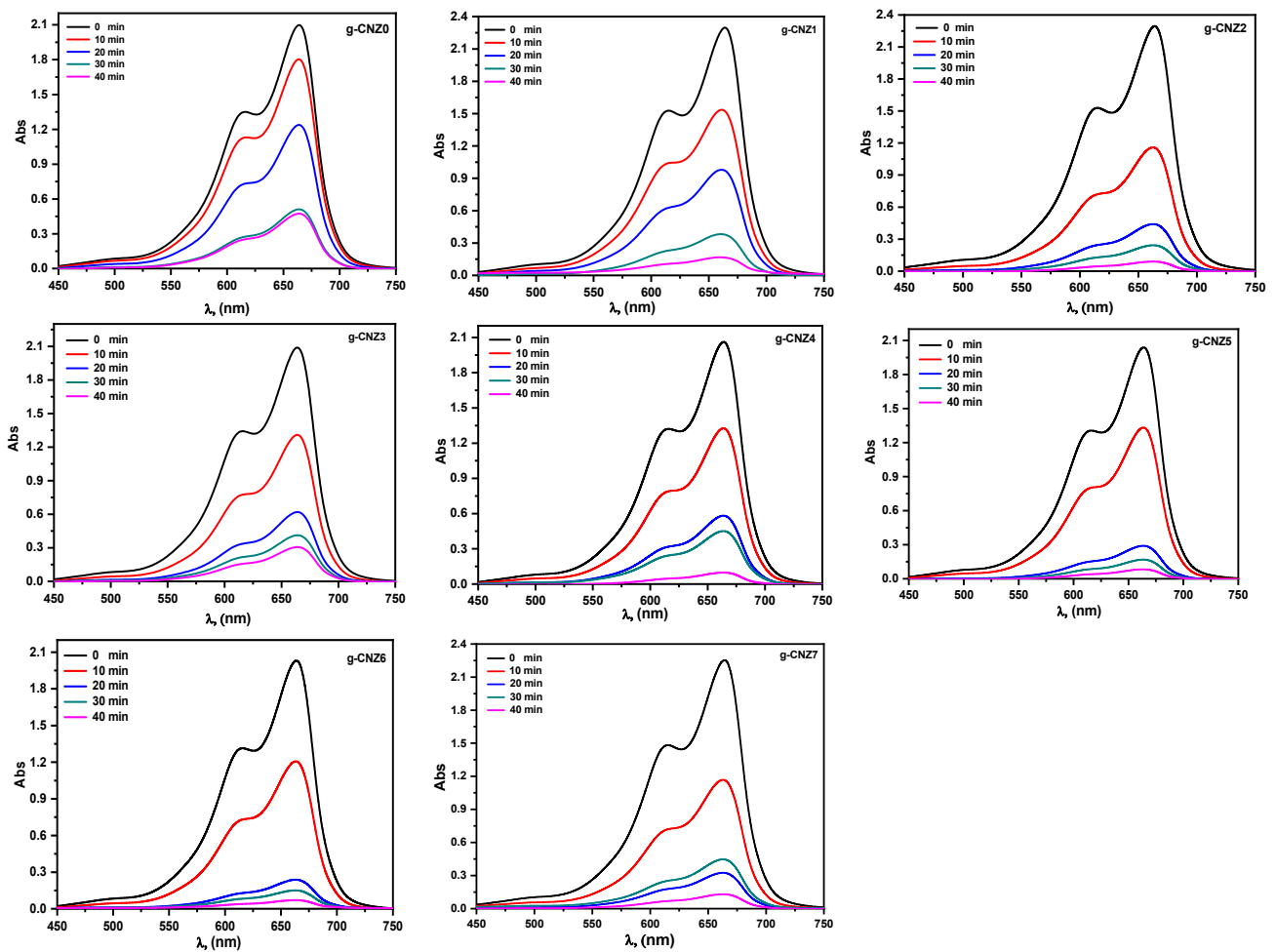


Figure 6. UV-vis absorption spectra of photocatalytic MB degradation over g-CNZ nanocomposite.

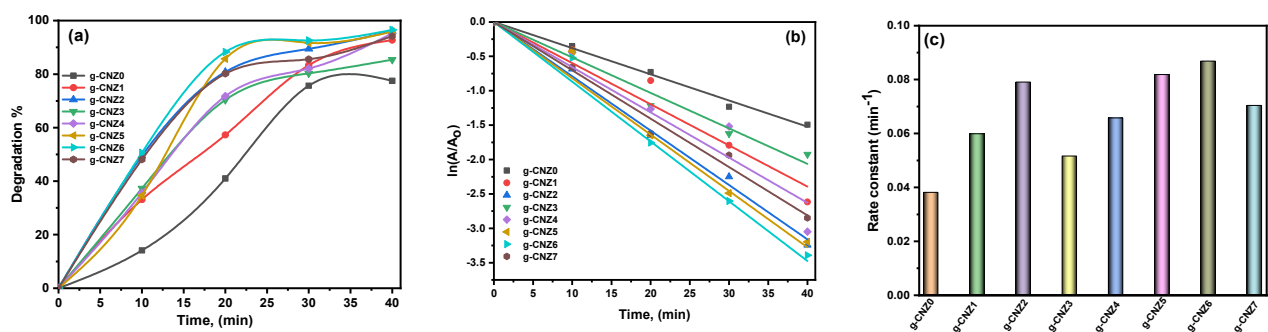


Figure 7. (a) Photodegradation efficiency toward MB, (b) the photocatalytic rate curves, and (c) the kinetics rate of the g-CNZ nanocomposite.

2.6.2. Photodegradation of Mixed Dye

Combining two organic dyes (MB and EY) made it possible to imitate the appearance of real water contamination. The only variation between the experimental setup and the setup for the individual contaminants was the extended adsorption–desorption duration of 30 min. The photocatalyst was dissolved in 200 mL of a solution containing 10 ppm of the MB and EY dye and 0.01 g of the photocatalyst. The results of the evaluation of the g-CNZ₆ photocatalyst's photocatalytic performance for the mixed pollutants are displayed in Figure 10. By observing the UV-vis maximum absorbance peaks of MB and EY at 664 nm and 518 nm, respectively, the photocatalytic performance of the g-CNZ₆ nanocomposite towards the matrix of the pollutant was assessed. As shown in Figure 10.

their maximum absorbance peaks diminish as the UVc light exposure time increases. At 120 min, photocatalytic rates of above 45% for MB and above 92% for EY were attained. Compared to other cationic dye pollutants (see Table 4), the g-CNZ₆ nanocomposite was more effective at removing anionic dyes. According to the above results, our g-CNZ₆ photocatalyst can be used in actual wastewater samples even if the better removal efficiency of those pollutants was only attained after a longer irradiation time.

Table 3. Degradation efficiency and kinetic rate of MB and EY dyes.

Photocatalyst	Methylene Blue		Eosine Yellow	
	Degradation (%)	K (min ⁻¹)	Degradation (%)	K (min ⁻¹)
g-CNZ ₀	77.5	0.035	91.8	0.0567
g-CNZ ₁	92.7	0.059	93.8	0.0696
g-CNZ ₂	96.09	0.079	91.3	0.0616
g-CNZ ₃	85.4	0.051	93.7	0.0665
g-CNZ ₄	95.2	0.065	93.6	0.0674
g-CNZ ₅	95.9	0.081	94.3	0.0730
g-CNZ ₆	96.5	0.088	95.6	0.0767
g-CNZ ₇	94.2	0.070	94.1	0.0684

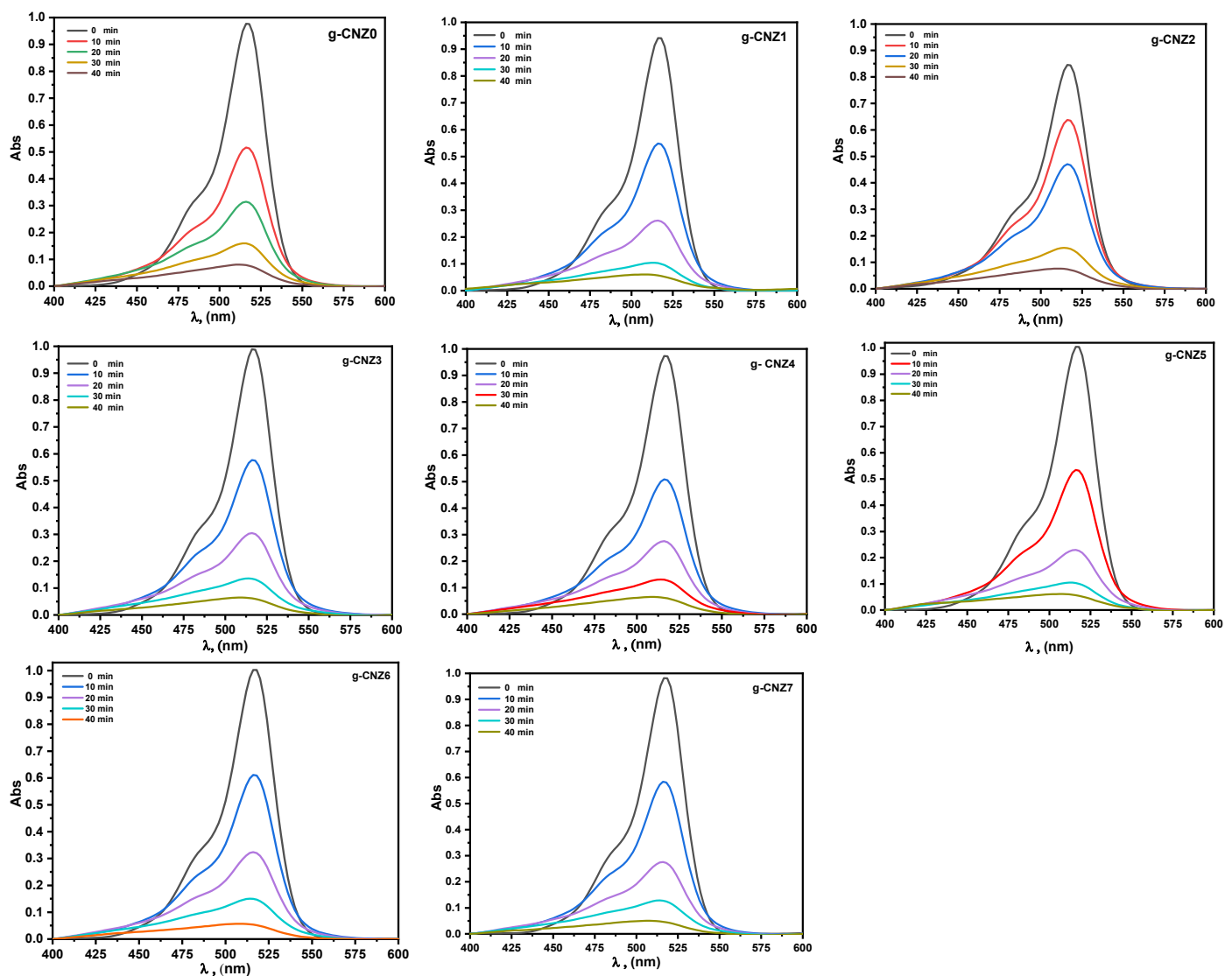


Figure 8. UV-vis absorption spectra of photocatalytic EY degradation over g-CNZ nanocomposite.

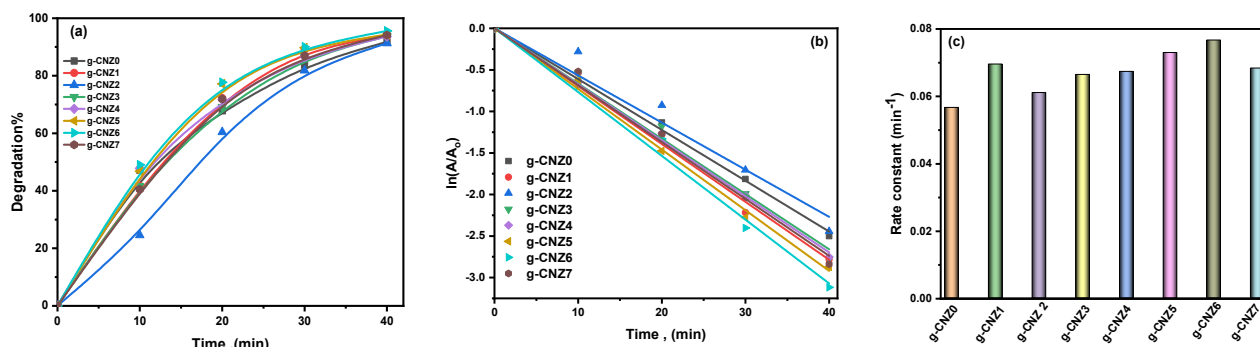


Figure 9. (a) Photodegradation efficiency toward EY, (b) the photocatalytic rate curves, and (c) kinetics rate of the g-CNZ nanocomposites.

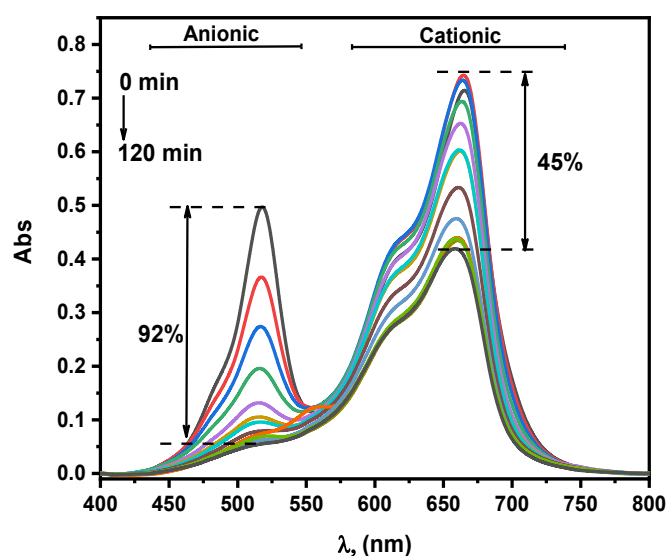


Figure 10. Photodegradation of organic dyes in the presence of g-CNZ₆ nanocomposite.

Table 4. Some g-C₃N₄/ZrO₂ composite photocatalysts and photodegradation efficiency of organic pollutants.

Photocatalyst	Dye	Catalyst Dose (g)	Dye Concentration (ppm)	Light Sources	Time (min)	Degradation Efficiency (%)	Rate Constant (min ⁻¹)	Refs.
ZrO ₂ /g-C ₃ N ₄	MB	0.2	50	Xenon lamp 300 W	210	99	0.8398	[60]
ZrO ₂ /g-C ₃ N ₄	MB	0.1	10	Visible light	75	89	0.0382	[61]
g-C ₃ N ₄ /ZrO ₂	RhB	0.6	10	Xenon lamp 300 W	150	82	-	[62]
g-C ₃ N ₄ /t-ZrO ₂	RhB	1	10	Xenon lamp 300 W	40	99.6	-	[63]
(2D/2D) g-C ₃ N ₄ /ZrO ₂	MB	0.3	10	Two LED lamps, 50 W	80	96.76	0.0114	[20]
g-C ₃ N ₄ /ZrO ₂	4-NP	0.6	30	Solar light	120	-	0.0167	[64]
g-C ₃ N ₄ /ZrO ₂	MB	0.01	10	λ = 225 nm	40	96.5	0.0881	Our study
	EY	0.01	10	UVc	40	95.6	0.0767	

2.6.3. Reactive Species Involved in Photodegradation of MB Dye by g-CNZ₆ Nanocomposites

To further understand the g-CNZ₆ nanocomposite's photocatalytic process, free radical capture studies were also conducted. As indicated in Figure 11, four scavengers were added to the pollutant solution before the photocatalytic experiment: isopropyl alcohol (IPA: ·OH), sodium chloride (NaCl: h⁺), ascorbic acid (ASC: O₂^{·-}), and sodium nitrate (NaNO₃: e⁻). The amount of MB degradation was not significantly impacted by ascorbic acid (ASC: O₂^{·-} scavenger). Since sodium chloride (NaCl) is a h⁺ scavenger, the degradation percentage dramatically decreases when it is introduced, going from 96.5 % to 20 %. The degradation percentage fell to 10% when ascorbic acid (ASC: O₂^{·-} scavenger) was present. This implies that h⁺ and O₂^{·-} are two important reactive species in the photodegradation of MB by the g-CNZ₆ nanocomposites.

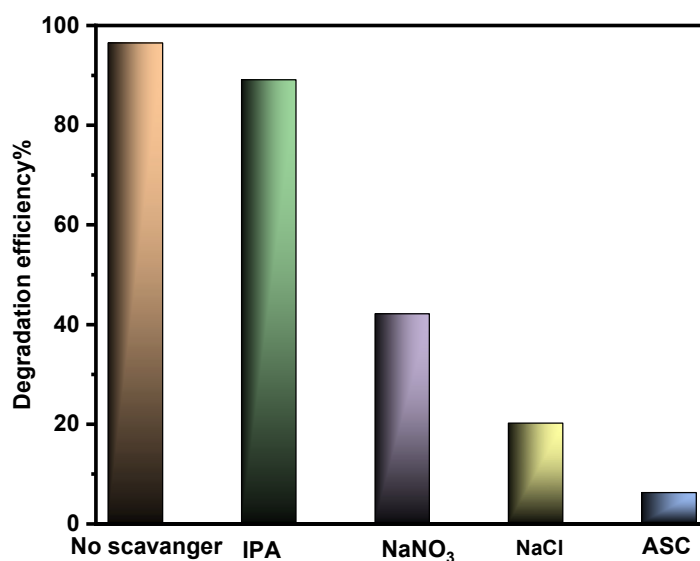


Figure 11. Scavenger of MB dye in the presence of g-CNZ₆ nanocomposite.

2.6.4. Possible Mechanistic Pathway for Degradation of MB Dye

The following formula describes how the active species in the chemical process in which the semiconductors VB and CB are involved are different [65,66]:

$$E_{CB} = X - E_0 - 0.5E_g \quad (5)$$

$$E_{VB} = E_{CB} + E_g \quad (6)$$

The E_g is the band gap, X is the absolute electronegativity, and the values of g-C₃N₄ and ZrO₂ for X are 4.73 eV and 5.91 eV, respectively. E_0 is a constant, regarding the standard H electrode with a value of 4.5 eV [67–69]. As a result, the predicted E_{CB} values for the CN nanosheet and ZrO₂ nanoparticle are -1.02 and -0.99 eV, respectively. Additionally, the E_{VB} of the samples of the CN nanosheets and ZrO₂ nanoparticles is $+1.49$ and $+3.81$ eV, respectively. Figure 12 delineates the anticipated method for Methylene Blue (MB) dye degradation by applying a g-CNZ₆ nanocomposite under ultraviolet C (UVC) light irradiation. The underpinning of this mechanism is derived from valence band (VB) and conduction band (CB) potentials, extrapolated from diffuse reflectance spectroscopy (DRS) analysis in conjunction with the results from active species experimentation.

The narrow bandgap of pure graphitic carbon nitride (g-C₃N₄) triggers the generation of electron–conduction band (e^-_{CB}) and hole–valence band (h^+_{VB}) pairs upon exposure to UVC light, a characteristic of individual semiconductors. However, the subsequent rapid recombination of these pairs results in limited photocatalytic activity in pure g-C₃N₄, attributable to its relatively small bandgap (2.51 eV). Conversely, the large bandgap of pure ZrO₂ nanoparticles, estimated at 4.8 eV, inhibits its excitation under UVC light expo-

sure [64]. Consequently, when UVc light is incident on the g-CNZ nanocomposite surface, the valence band (VB) electrons in both semiconductor constituents (g-C₃N₄ and ZrO₂) are instantaneously excited to their respective conduction bands (CBs), leaving behind holes in the VB. The disparity in CB edge potentials between the two materials, with g-C₃N₄ exhibiting a more negative potential than ZrO₂, facilitates the migration of photoexcited electrons from the CB of g-C₃N₄ to the CB of ZrO₂. The resultant electrons reside at the CB of ZrO₂, instigating interactions with surface oxygen to form superoxide radicals (O₂^{•-}), which subsequently interact with MB. Simultaneously, photogenerated holes at the VB of ZrO₂ migrate to the VB of g-C₃N₄ due to the higher VB potential of ZrO₂ than g-C₃N₄. Consequently, these newly formed holes remain in the VB of g-C₃N₄, where they instigate their reactions with MB. The formation of a type II heterojunction significantly decreases the recombination rate while promoting the separation of photoinduced electrons and holes at the interface between g-C₃N₄ and ZrO₂. The photocarriers at the g-C₃N₄@ZrO₂ interfaces still maintain the Z-scheme transfer mechanism, like in the case of bare photocatalysis. More interestingly, under the action of the polarization field, the bulk photoelectrons of g-C₃N₄ and ZrO₂ are driven to Z-scheme transfer [65]. The efficiency of the charge transport and separation of electron–hole pairs is contingent on the interaction between ZrO₂ and g-C₃N₄. An excess of ZrO₂ can accumulate on the g-C₃N₄ layer, diminishing the interaction between the two materials and thus compromising the charge separation efficiency. As such, an optimal ZrO₂ concentration is deemed crucial. The anticipated mechanism for the degradation of MB by the g-CNZ₆ nanocomposite, as represented in Equations (9)–(13), can be described as follows:

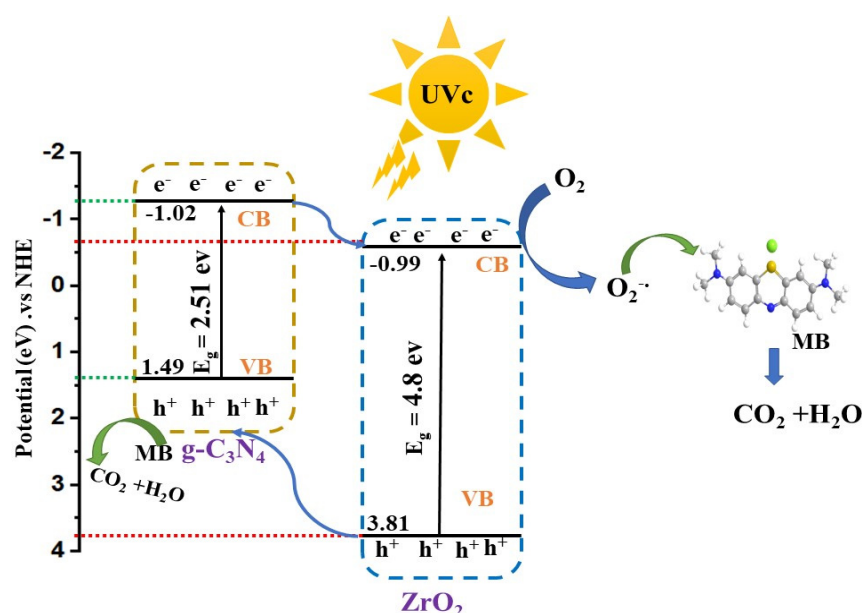
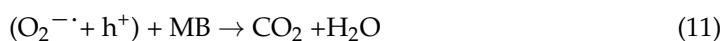
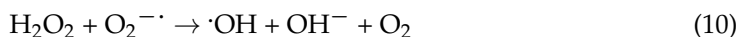
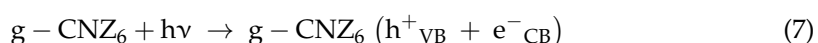


Figure 12. A possible mechanism for degradation of MB in UVc by MB by g-CNZ₆ nanocomposite.

2.6.5. Stability and Recycling

Repeated assessments were executed on M) degradation, extending up to the fifth cycle to validate the scalability of the synthesized g-CNZ₆ nanocomposite. Following each

cycle, the photocatalyst was retrieved through centrifugation, rinsed with distilled water, and dried in an oven set at a temperature of 80 °C. Figure 13 illustrates a marginal reduction in the photocatalytic efficacy of the g-CNZ₆ nanocomposite towards MB photodegradation. However, despite this slight decrement in performance, it was demonstrated that the g-CNZ₆ nanocomposite maintains considerable photocatalytic activity over multiple iterations. This observed resilience solidifies g-CNZ₆'s position as a competent photocatalyst. The composite can be recycled and reused multiple times while demonstrating substantial activity in a photocatalytic reaction, reinforcing its potential for sustained utilization.

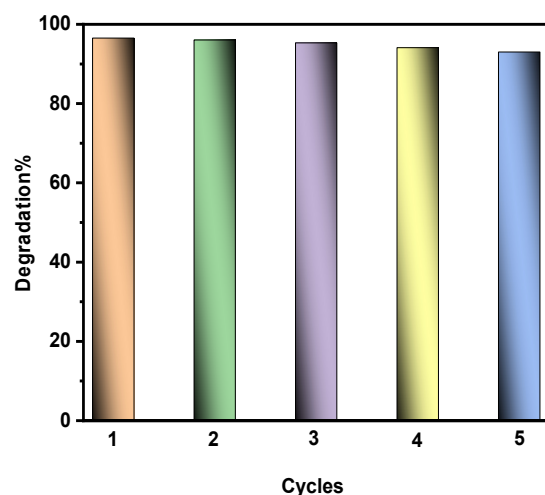


Figure 13. Reusability curve for degradation of MB by g-CNZ₆ nanocomposite.

3. Experimental Section

3.1. Materials

Zirconium oxychloride ($\text{ZrOCl}_2 \cdot 8\text{H}_2\text{O}$) was procured from Alpha Chem (Darmstadt, Germany). Urea, thiourea, methylene blue (MB), and eosin yellow (EY) were obtained from Merck (Darmstadt, Germany). Double distilled water (DDW) was employed in the preparation of samples.

3.2. Preparation of g-C₃N₄@ZrO₂

Porous graphitic carbon nitride (g-CN) was prepared via thermal polycondensation of urea. A predefined amount of 6 g from urea and thiourea was finely ground and placed in a closed crucible and subjected to a controlled heating regimen at a rate of 5 °C/min up to a final temperature of 550 °C, which was maintained for post-cooling to ambient cycles, and the product was finely ground in an agate mortar.

The synthesis of g-C₃N₄@ZrO₂ nanocomposites was conducted following the protocol illustrated in Figure 14. A total of 0.5 g from g-C₃N₄ was added to 50 mL DDW and placed in an ultrasonic probe for 15 min. A homogenous mixture was created by adding 10 g of Zirconium oxychloride to 10 g of citric acid, into which specific proportions of ZrO₂ was added, and was stirred for 30 min to establish homogeneity in the resulting solution. This mixture was subsequently dried at 100 °C for 24 h. The dried composite was then calcinated at 550 °C for 2 h in a muffle furnace and later crushed to a uniform powder. The final composites, bearing different proportions of ZrO₂ (0.001, 0.005, 0.01, 0.05, 0.1, 0.5, and 1 g), were designated as g-CNZ₀ through g-CNZ₇, respectively.

3.3. Characterization Techniques and Devices

X-ray diffraction (XRD) was employed to determine the crystalline structure of the synthesized photocatalysts. Scanning electron microscopy (SEM, model JSM-6360, Tokyo, Japan) operating at 20 kV, supplemented with energy-dispersive X-ray spectroscopy (EDX), was used to probe the surface morphology and elemental composition. The functional

chemical bonds were identified from FT-IR Perkin Elme(Waltham, MA, USA) r in the range of 4000 to 400 cm^{-1} wavenumber. The optical properties were observed using UV-visible DRS (JASCO V-570, Tokyo, Japan).

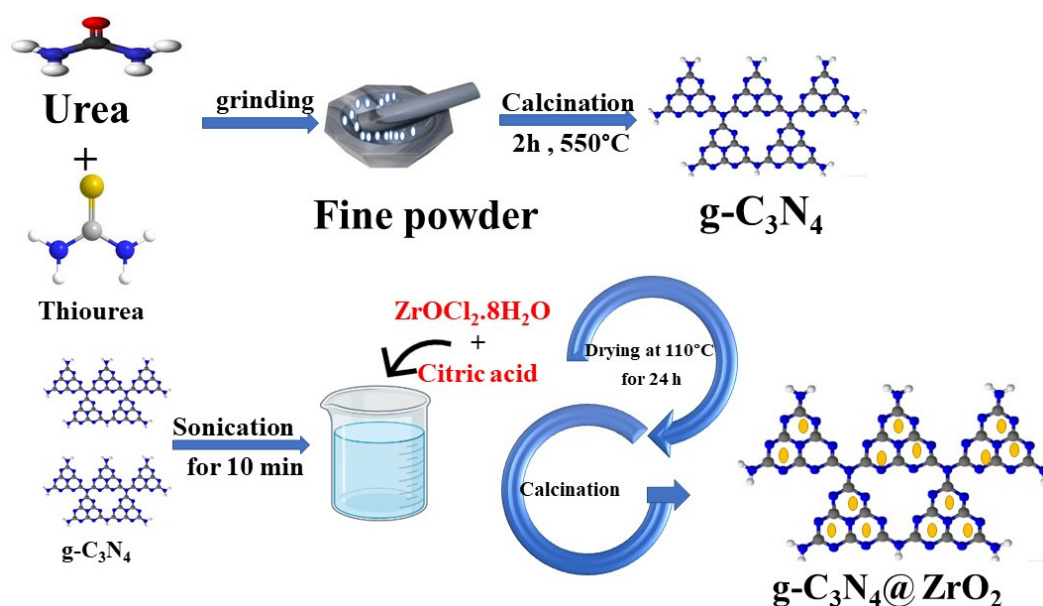


Figure 14. Schematic route of the synthesis pathway of the $\text{g-C}_3\text{N}_4@ZrO_2$ NCs.

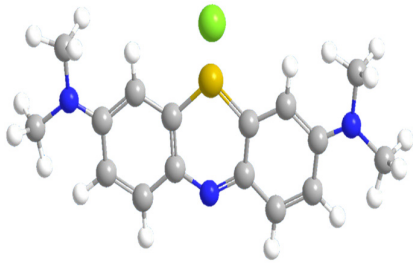
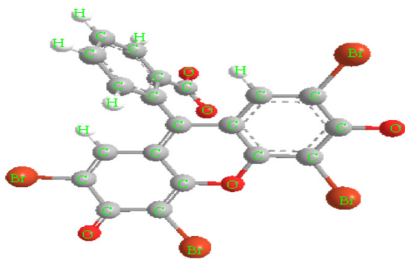
3.4. Photoreactor Design and Photocatalytic Activity of $\text{g-C}_3\text{N}_4@ZrO_2$ Nanocomposites for Photodegradation

The photocatalytic performance of the synthesized $\text{g-C}_3\text{N}_4@ZrO_2$ nanocomposites was measured under UVC radiation for the model pollutant using a wooden photoreactor at room temperature, designed by I.S. Yahia and his group at NLEBA/ASU/Egypt; more details about the photoreactor are mentioned in Hussien et al. [70]. The dyes methylene blue (MB) and eosin yellow (EY) were employed as contaminants for this assessment. The structure, chemical formula and type are shown in Table 5. A total of 0.01 g of each composite was dispersed in a 200 mL solution containing either dye at a concentration of 10 ppm, and the mixture was subjected to dark conditions for approximately 30 min to attain adsorption–desorption equilibrium. After this period, samples were extracted and centrifuged at 3000 rpm for 10 min, and the residual mixture was re-illuminated using UVC lamps. Photocatalytic activity was quantified at intervals of 10 min during irradiation, and photodegradation was monitored within the range of 400 to 800 nm using a UV-Vis spectrophotometer (Agilent, Santa Clara, CA, USA). Degradation efficiency and apparent rate constants were calculated using Equations (1) and (2) [71]; the degree of dye degradation, apparent degradation rate constant (k_{app}) in min^{-1} , and photodegradation efficiency ($PDE\%$) were systematically calculated. A_0 and A denote the dye concentration at the initial time and at a desired time t post-irradiation, respectively.

$$PDE\% = \frac{A_0 - A}{A_0} \times 100\% \quad (12)$$

$$\ln \left(\frac{A}{A_0} \right) = -Kt \quad (13)$$

Table 5. Characteristics of Methylene Blue (MB) and Eosin Yellow (EY) dyes.

Characteristics	Methylene Blue	Eosin Yellow
Structure:		
Chemical Formula:	$C_{16}H_{18}N_3S Cl$	$C_{20}H_8Br_4NaO_5$
Type of dye:	Cationic dye	Anionic dye

4. Conclusions

In this investigation, we have developed an augmented photocatalyst, a g-C₃N₄@ZrO₂ composite, exhibiting an amplified response to direct UVC light exposure, synthesized via a simple pyrolysis process of fabricated g-C₃N₄@ZrO₂ samples, complemented by sonication. Upon exposure to direct UVC radiation, the g-CNZ₆ nanocomposite demonstrated superior photocatalytic efficacy in degraded MB, EY, and a mixed dye. Compared to the pure g-C₃N₄, the degradation efficiency of the g-CNZ₆ nanocomposite was remarkably higher, with respective yields of 96.5% and 95.6% for the MB and EY dyes. This significant increase in the photocatalytic performance can be attributed to the synergistic interaction between ZrO₂ and g-C₃N₄, culminating in efficient electron–hole pair separation, a critical driver of photocatalysis. An extensive series of reusability experiments unveiled that the g-CNZ₆ nanocomposite maintained its photocatalytic stability and robustness, indicating promising potential for sustainable applications in dye degradation and water treatment.

Author Contributions: Conceptualization, A.T.M., F.F.A.-H., S.M.G., H.Y.Z., M.S.A.H. and I.S.Y.; Methodology, A.T.M., F.F.A.-H., S.M.G., S.H.Z., H.Y.Z. and I.S.Y.; Software, A.T.M., F.F.A.-H., S.M.G., S.H.Z., M.S.A.H. and I.S.Y.; Resources, F.F.A.-H. and S.M.G.; Writing—original draft, A.T.M., F.F.A.-H., S.M.G., S.H.Z., H.Y.Z., M.S.A.H. and I.S.Y.; Writing—review & editing, A.T.M., F.F.A.-H., S.M.G., S.H.Z., H.Y.Z., M.S.A.H. and I.S.Y.; Visualization, A.T.M., F.F.A.-H., S.M.G., S.H.Z., H.Y.Z. and I.S.Y.; Supervision, F.F.A.-H., S.M.G. and I.S.Y.; Project administration, F.F.A.-H., S.M.G. and I.S.Y.; Funding acquisition, F.F.A.-H. and S.M.G. All authors have read and agreed to the published version of the manuscript.

Funding: This research project was funded by the Deanship of Scientific Research, Princess Nourah bint Abdulrahman University, through the program of research project funding after publication, grant NO. 44-PRFA-P-100.

Data Availability Statement: Data are contained within the article.

Conflicts of Interest: The author Ahmed T. Mosleh was employed by the Egyptian Company for Carbon Materials. The remaining authors declare that the research was conducted in the absence of any commercial or financial relationships that could be construed as a potential conflict of interest.

References

- Shwetharani, R.; Chandan, H.; Sakar, M.; Balakrishna, G.R.; Reddy, K.R.; Raghu, A.V. Photocatalytic semiconductor thin films for hydrogen production and environmental applications. *Int. J. Hydrogen Energy* **2020**, *45*, 18289–18308. [[CrossRef](#)]
- Vickers, N.J. Animal communication: When I am calling you, will you answer too? *Curr. Biol.* **2017**, *27*, R713–R715. [[CrossRef](#)] [[PubMed](#)]
- Ali, A.; Ahmed, A.; Usman, M.; Raza, T.; Ali, M.S.; Al-Nahari, A.; Liu, C.; Li, D.; Li, C.J.D.; Materials, R. Synthesis of visible light responsive Ce_{0.2}Co_{0.8}Fe₂O₄/g-C₃N₄ composites for efficient photocatalytic degradation of rhodamine B. *Diam. Relat. Mater.* **2023**, *133*, 109721. [[CrossRef](#)]

4. Li, L.; Sun, X.; Xian, T.; Gao, H.; Wang, S.; Yi, Z.; Wu, X.; Yang, H. Template-free synthesis of Bi₂O₂C₃ hierarchical nanotubes self-assembled from ordered nanoplates for promising photocatalytic applications. *Phys. Chem. Chem. Phys.* **2022**, *24*, 8279–8295. [[CrossRef](#)] [[PubMed](#)]
5. Cheng, T.; Gao, H.; Liu, G.; Pu, Z.; Wang, S.; Yi, Z.; Wu, X.; Yang, H.J.C.; Physicochemical, S.A.; Aspects, E. Preparation of core-shell heterojunction photocatalysts by coating CdS nanoparticles onto Bi₄Ti₃O₁₂ hierarchical microspheres and their photocatalytic removal of organic pollutants and Cr (VI) ions. *Colloids Surf. A Physicochem. Eng. Asp.* **2022**, *633*, 127918. [[CrossRef](#)]
6. Saravanan, A.; Kumar, P.S.; Jeevanantham, S.; Karishma, S.; Tajsabreen, B.; Yaashikaa, P.; Reshma, B.J.C. Effective water/wastewater treatment methodologies for toxic pollutants removal: Processes and applications towards sustainable development. *Chemosphere* **2021**, *280*, 130595. [[CrossRef](#)] [[PubMed](#)]
7. Zhang, S.; Li, B.; Wang, X.; Zhao, G.; Hu, B.; Lu, Z.; Wen, T.; Chen, J.; Wang, X. Recent developments of two-dimensional graphene-based composites in visible-light photocatalysis for eliminating persistent organic pollutants from wastewater. *Chem. Eng. J.* **2020**, *390*, 124642. [[CrossRef](#)]
8. Yang, X.; Zhou, J.; Huo, T.; Lv, Y.; Pan, J.; Chen, L.; Tang, X.; Zhao, Y.; Liu, H.; Gao, Q.; et al. Metabolic insights into the enhanced nitrogen removal of anammox by montmorillonite at reduced temperature. *Chem. Eng. J.* **2021**, *410*, 128290. [[CrossRef](#)]
9. Lim, J.; Kim, H.; Park, J.; Moon, G.-H.; Vequizo, J.J.M.; Yamakata, A.; Lee, J.; Choi, W. How g-C₃N₄ works and is different from TiO₂ as an environmental photocatalyst: Mechanistic view. *Environ. Sci. Technol.* **2019**, *54*, 497–506. [[CrossRef](#)]
10. Hoffmann, M.R.; Martin, S.T.; Choi, W.; Bahnemann, D.W. Environmental applications of semiconductor photocatalysis. *Chem. Rev.* **1995**, *95*, 69–96. [[CrossRef](#)]
11. Habibollahi, Z.; Peyravi, M.; Khalili, S.; Jahanshahi, M. ZnO-based ternary nanocomposite for decolorization of methylene blue by photocatalytic dynamic membrane. *Mater. Today Chem.* **2022**, *23*, 100748. [[CrossRef](#)]
12. Kazemi, M.; Peyravi, M.; Jahanshahi, M. Multilayer UF membrane assisted by photocatalytic NZVI@ TiO₂ nanoparticle for removal and reduction of hexavalent chromium. *J. Water Process Eng.* **2020**, *37*, 101183. [[CrossRef](#)]
13. Kazemi, M.; Jahanshahi, M.; Peyravi, M. Hexavalent chromium removal by multilayer membrane assisted by photocatalytic couple nanoparticle from both permeate and retentate. *J. Hazard. Mater.* **2018**, *344*, 12–22. [[CrossRef](#)] [[PubMed](#)]
14. Kazemi, M.; Jahanshahi, M.; Peyravi, M. Chitosan-sodium alginate multilayer membrane developed by Fe⁰@ WO₃ nanoparticles: Photocatalytic removal of hexavalent chromium. *Carbohydr. Polym.* **2018**, *198*, 164–174. [[CrossRef](#)]
15. Zakeritabar, S.F.; Jahanshahi, M.; Peyravi, M.; Akhtari, J. Engineering, Photocatalytic study of nanocomposite membrane modified by CeF₃ catalyst for pharmaceutical wastewater treatment. *J. Environ. Health Sci.* **2020**, *18*, 1151–1161.
16. Luo, W.; Chen, X.; Wei, Z.; Liu, D.; Yao, W.; Zhu, Y. Three-dimensional network structure assembled by g-C₃N₄ nanorods for improving visible-light photocatalytic performance. *Appl. Catal. B Environ.* **2019**, *255*, 117761. [[CrossRef](#)]
17. Chen, Y.; Lu, W.; Shen, H.; Gu, Y.; Xu, T.; Zhu, Z.; Wang, G.; Chen, W. Solar-driven efficient degradation of emerging contaminants by g-C₃N₄-shielding polyester fiber/TiO₂ composites. *Appl. Catal. B Environ.* **2019**, *258*, 117960. [[CrossRef](#)]
18. Singla, S.; Sharma, S.; Basu, S.; Shetti, N.P.; Reddy, K.R. Graphene/graphitic carbon nitride-based ternary nanohybrids: Synthesis methods, properties, and applications for photocatalytic hydrogen production. *FlatChem* **2020**, *24*, 100200. [[CrossRef](#)]
19. Naseri, A.; Samadi, M.; Pourjavadi, A.; Moshfegh, A.Z.; Ramakrishna, S. Graphitic carbon nitride (g-C₃N₄)-based photocatalysts for solar hydrogen generation: Recent advances and future development directions. *J. Mater. Chem. A* **2017**, *5*, 23406–23433. [[CrossRef](#)]
20. Tanzifi, M.; Jahanshahi, M.; Peyravi, M.; Khalili, S. A morphological decoration of g-C₃N₄/ZrO₂ heterojunctions as a visible light activated photocatalyst for degradation of various organic pollutants. *J. Environ. Chem. Eng.* **2022**, *10*, 108600. [[CrossRef](#)]
21. Liao, G.; Chen, S.; Quan, X.; Yu, H.; Zhao, H. Graphene oxide modified g-C₃N₄ hybrid with enhanced photocatalytic capability under visible light irradiation. *J. Mater. Chem.* **2012**, *22*, 2721–2726. [[CrossRef](#)]
22. Panimalar, S.; Uthrakumar, R.; Selvi, E.T.; Gomathy, P.; Inmozhi, C.; Kaviyarasu, K.; Kennedy, J. Studies of MnO₂/g-C₃N₄ heterostructure efficient of visible light photocatalyst for pollutants degradation by sol-gel technique. *Surf. Interfaces* **2020**, *20*, 100512. [[CrossRef](#)]
23. Zhang, W.; Xu, D.; Wang, F.; Chen, M. AgCl/Au/g-C₃N₄ ternary composites: Efficient photocatalysts for degradation of anionic dyes. *J. Alloys Compd.* **2021**, *868*, 159266. [[CrossRef](#)]
24. Xu, X.; Wang, J.; Shen, Y. An interface optimization strategy for g-C₃N₄-based S-scheme heterojunction photocatalysts. *Langmuir* **2021**, *37*, 7254–7263. [[CrossRef](#)] [[PubMed](#)]
25. Preeyanghaa, M.; Vinesh, V.; Neppolian, B. Construction of S-scheme 1D/2D rod-like g-C₃N₄/V₂O₅ heterostructure with enhanced sonophotocatalytic degradation for Tetracycline antibiotics. *Chemosphere* **2022**, *287*, 132380. [[CrossRef](#)] [[PubMed](#)]
26. Du, H.; Liu, Y.-N.; Shen, C.-C.; Xu, A.-W. Nanoheterostructured photocatalysts for improving photocatalytic hydrogen production. *Chin. J. Catal.* **2017**, *38*, 1295–1306. [[CrossRef](#)]
27. Jiang, G.; Zheng, C.; Yan, T.; Jin, Z. Cd_{0.8}Mn_{0.2}S/MoO₃ composites with an S-scheme heterojunction for efficient photocatalytic hydrogen evolution. *Dalton Trans.* **2021**, *50*, 5360–5369. [[CrossRef](#)] [[PubMed](#)]
28. Li, Y.; Zhou, M.; Cheng, B.; Shao, Y. Recent advances in g-C₃N₄-based heterojunction photocatalysts. *J. Mater. Sci. Technol.* **2020**, *56*, 1–17. [[CrossRef](#)]
29. Tian, N.; Huang, H.; He, Y.; Guo, Y.; Zhang, T.; Zhang, Y. Mediator-free direct Z-scheme photocatalytic system: BiVO₄/g-C₃N₄ organic-inorganic hybrid photocatalyst with highly efficient visible-light-induced photocatalytic activity. *Dalton Trans.* **2015**, *44*, 4297–4307. [[CrossRef](#)] [[PubMed](#)]

30. Yu, J.; Wang, S.; Low, J.; Xiao, W. Enhanced photocatalytic performance of direct Z-scheme g-C₃N₄-TiO₂ photocatalysts for the decomposition of formaldehyde in air. *Phys. Chem. Chem. Phys.* **2013**, *15*, 16883–16890. [[CrossRef](#)]
31. Low, J.; Yu, J.; Jaroniec, M.; Wageh, S.; Al-Ghamdi, A.A. Heterojunction photocatalysts. *Adv. Mater.* **2017**, *29*, 1601694. [[CrossRef](#)]
32. Zhang, H.; Tang, G.; Wan, X.; Xu, J.; Tang, H. High-efficiency all-solid-state Z-scheme Ag₃PO₄/g-C₃N₄/MoSe₂ photocatalyst with boosted visible-light photocatalytic performance for antibiotic elimination. *Appl. Surf. Sci.* **2020**, *530*, 147234. [[CrossRef](#)]
33. Hu, L.; Hu, H.; Lu, W.; Lu, Y.; Wang, S. Novel composite BiFeO₃/ZrO₂ and its high photocatalytic performance under white LED visible-light irradiation. *Mater. Res. Bull.* **2019**, *120*, 110605. [[CrossRef](#)]
34. Bhaskaruni, S.V.; Maddila, S.; van Zyl, W.E.; Jonnalagadda, S.B. V₂O₅/ZrO₂ as an efficient reusable catalyst for the facile, green, one-pot synthesis of novel functionalized 1,4-dihydropyridine derivatives. *Catal. Today* **2018**, *309*, 276–281. [[CrossRef](#)]
35. Botta, S.G.; Navío, J.A.; Hidalgo, M.C.; Restrepo, G.M.; Litter, M.I. Photocatalytic properties of ZrO₂ and Fe/ZrO₂ semiconductors prepared by a sol-gel technique. *J. Photochem. Photobiol. A Chem.* **1999**, *129*, 89–99. [[CrossRef](#)]
36. Fil, B.A.; Özmetin, C.; Korkmaz, M. Cationic dye (methylene blue) removal from aqueous solution by montmorillonite. *Bull. Korean Chem. Soc.* **2012**, *33*, 3184–3190. [[CrossRef](#)]
37. Ndlovu, T.; Kuvarega, A.T.; Arotiba, O.A.; Sampath, S.; Krause, R.W.; Mamba, B.B. Exfoliated graphite/titanium dioxide nanocomposites for photodegradation of eosin yellow. *Appl. Surf. Sci.* **2014**, *300*, 159–164. [[CrossRef](#)]
38. Vellaichamy, B.; Periakaruppan, P. Ag nanoshell catalyzed dedying of industrial effluents. *RSC Adv.* **2016**, *6*, 31653–31660. [[CrossRef](#)]
39. Hussien, M.S.; Mohammed, M.I.; Yahia, I.S. Flexible photocatalytic membrane based on CdS/PMMA polymeric nanocomposite films: Multifunctional materials. *Environ. Sci. Pollut. Res.* **2020**, *27*, 45225–45237. [[CrossRef](#)]
40. Hu, L.; Li, M.; Cheng, L.; Jiang, B.; Ai, J. Solvothermal synthesis of octahedral and magnetic CoFe₂O₄-reduced graphene oxide hybrids and their photo-Fenton-like behavior under visible-light irradiation. *RSC Adv.* **2021**, *11*, 22250–22263. [[CrossRef](#)]
41. Lin, B.; Li, H.; An, H.; Hao, W.; Wei, J.; Dai, Y.; Ma, C.; Yang, G. Preparation of 2D/2D g-C₃N₄ nanosheet@ZnIn₂S₄ nanoleaf heterojunctions with well-designed high-speed charge transfer nanochannels towards high-efficiency photocatalytic hydrogen evolution. *Appl. Catal. B Environ.* **2018**, *220*, 542–552. [[CrossRef](#)]
42. Markgraf, S.; Reader, J. Calculated from ICSD using POWD-12++,(1997). *Mineral* **1985**, *70*, 590.
43. Hann, R.E.; Suitch, P.R.; Pentecost, J.L. Monoclinic crystal structures of ZrO₂ and HfO₂ refined from X-ray powder diffraction data. *J. Am. Ceram. Soc.* **1985**, *68*, C-285–C-286. [[CrossRef](#)]
44. Bindu, P.; Thomas, S. Estimation of lattice strain in ZnO nanoparticles: X-ray peak profile analysis. *J. Theor. Appl. Phys.* **2014**, *8*, 123–134. [[CrossRef](#)]
45. Bi, X.; Yu, S.; Liu, E.; Yin, X.; Zhao, Y.; Xiong, W. Nano-zirconia supported by graphitic carbon nitride for enhanced visible light photocatalytic activity. *RSC Adv.* **2020**, *10*, 524–532. [[CrossRef](#)] [[PubMed](#)]
46. Li, C.; Sun, Z.; Zhang, W.; Yu, C.; Zheng, S. Highly efficient g-C₃N₄/TiO₂/kaolinite composite with novel three-dimensional structure and enhanced visible light responding ability towards ciprofloxacin and *S. aureus*. *Appl. Catal. B Environ.* **2018**, *220*, 272–282. [[CrossRef](#)]
47. Chand, S.; Mondal, A. g-C₃N₄/ZrO₂ composite material: A pre-eminent visible light-mediated photocatalyst for rhodamine B degradation in the presence of natural sunlight. *Ceram. Int.* **2023**, *49*, 5419–5430. [[CrossRef](#)]
48. Zhang, X.; Wang, X.; Meng, J.; Liu, Y.; Ren, M.; Guo, Y.; Yang, Y. Robust Z-scheme g-C₃N₄/WO₃ heterojunction photocatalysts with morphology control of WO₃ for efficient degradation of phenolic pollutants. *Sep. Purif. Technol.* **2021**, *255*, 117693. [[CrossRef](#)]
49. Bumajdad, A.; Nazeer, A.A.; Al Sagheer, F.; Nahar, S.; Zaki, M.I. Controlled synthesis of ZrO₂ nanoparticles with tailored size, morphology and crystal phases via organic/inorganic hybrid films. *Sci. Rep.* **2018**, *8*, 3695. [[CrossRef](#)]
50. Yan, H.; Yang, H. TiO₂-g-C₃N₄ composite materials for photocatalytic H₂ evolution under visible light irradiation. *J. Alloys Compd.* **2011**, *509*, L26–L29. [[CrossRef](#)]
51. Bai, X.; Wang, L.; Zong, R.; Zhu, Y. Photocatalytic activity enhanced via g-C₃N₄ nanoplates to nanorods. *J. Phys. Chem. C* **2013**, *117*, 9952–9961. [[CrossRef](#)]
52. Sayama, K.; Arakawa, H. Photocatalytic decomposition of water and photocatalytic reduction of carbon dioxide over zirconia catalyst. *J. Phys. Chem.* **1993**, *97*, 531–533. [[CrossRef](#)]
53. Zhang, Q.; Zhang, Y.; Li, H.; Gao, C.; Zhao, Y. Heterogeneous CaO-ZrO₂ acid-base bifunctional catalysts for vapor-phase selective dehydration of 1,4-butanediol to 3-buten-1-ol. *Appl. Catal. A Gen.* **2013**, *466*, 233–239. [[CrossRef](#)]
54. Xu, M.; Han, L.; Dong, S. Facile fabrication of highly efficient g-C₃N₄/Ag₂O heterostructured photocatalysts with enhanced visible-light photocatalytic activity. *ACS Appl. Mater. Interfaces* **2013**, *5*, 12533–12540. [[CrossRef](#)]
55. Zhao, Y.; Zhang, Y.; Li, J.; Du, X. Solvothermal synthesis of visible-light-active N-modified ZrO₂ nanoparticles. *Mater. Lett.* **2014**, *130*, 139–142. [[CrossRef](#)]
56. Jiang, D.; Wang, T.; Xu, Q.; Li, D.; Meng, S.; Chen, M. Perovskite oxide ultrathin nanosheets/g-C₃N₄ 2D-2D heterojunction photocatalysts with significantly enhanced photocatalytic activity towards the photodegradation of tetracycline. *Appl. Catal. B Environ.* **2017**, *201*, 617–628. [[CrossRef](#)]
57. Chen, Q.; Yang, W.; Zhu, J.; Fu, L.; Li, D.; Zhou, L. Enhanced visible light photocatalytic activity of g-C₃N₄ decorated ZrO₂-x nanotubes heterostructure for degradation of tetracycline hydrochloride. *J. Hazard. Mater.* **2020**, *384*, 121275. [[CrossRef](#)] [[PubMed](#)]
58. Bailón-García, E.; Elmouwahidi, A.; Carrasco-Marín, F.; Pérez-Cadenas, A.F.; Maldonado-Hódar, F.J. Development of Carbon-ZrO₂ composites with high performance as visible-light photocatalysts. *Appl. Catal. B Environ.* **2017**, *217*, 540–550. [[CrossRef](#)]

59. Reddy, C.V.; Reddy, K.R.; Shetti, N.P.; Shim, J.; Aminabhavi, T.M.; Dionysiou, D.D. Hetero-nanostructured metal oxide-based hybrid photocatalysts for enhanced photoelectrochemical water splitting—A review. *Int. J. Hydrogen Energy* **2020**, *45*, 18331–18347. [[CrossRef](#)]
60. Ke, Y.; Guo, H.; Wang, D.; Chen, J.; Weng, W. ZrO₂/g-C₃N₄ with enhanced photocatalytic degradation of methylene blue under visible light irradiation. *J. Mater. Res.* **2014**, *29*, 2473–2482. [[CrossRef](#)]
61. Ahilandeswari, G.; Arivuoli, D. Enhanced sunlight-driven photocatalytic activity in assembled ZrO₂/g-C₃N₄ nanocomposite. *J. Mater. Sci. Mater. Electron.* **2022**, *33*, 23986–24002. [[CrossRef](#)]
62. Zhang, K.; Zhou, M.; Yu, C.; Yang, K.; Li, X.; Dai, W.; Guan, J.; Shu, Q.; Huang, W. Construction of S-scheme g-C₃N₄/ZrO₂ heterostructures for enhancing photocatalytic disposals of pollutants and electrocatalytic hydrogen evolution. *Dyes Pigment.* **2020**, *180*, 108525. [[CrossRef](#)]
63. Zhou, M.; Wu, Y.; Shi, L.; Hu, S.; Li, H.; Gong, Y.; Niu, L.; Liu, X.; Li, C. Excellent Photocatalytic Efficiency of t-ZrO₂/g-C₃N₄ Photocatalyst for Pollutants Degradation: Experiment and theory. *Solid State Sci.* **2020**, *104*, 106202. [[CrossRef](#)]
64. Zarei, M.; Bahrami, J.; Zarei, M. Zirconia nanoparticle-modified graphitic carbon nitride nanosheets for effective photocatalytic degradation of 4-nitrophenol in water. *Appl. Water Sci.* **2019**, *9*, 175. [[CrossRef](#)]
65. Sun, X.; Xu, T.; Xian, T.; Yi, Z.; Liu, G.; Dai, J.; Yang, H. Insight on the enhanced piezo-photocatalytic mechanism of In₂O₃/BiFeO₃ heterojunctions for degradation of tetracycline hydrochloride. *Appl. Surf. Sci.* **2023**, *640*, 158408. [[CrossRef](#)]
66. Luo, J.; Zhou, X.; Ma, L.; Xu, X. Enhancing visible-light photocatalytic activity of g-C₃N₄ by doping phosphorus and coupling with CeO₂ for the degradation of methyl orange under visible light irradiation. *RSC Adv.* **2015**, *5*, 68728–68735. [[CrossRef](#)]
67. Wang, X.; Zhang, L.; Lin, H.; Nong, Q.; Wu, Y.; Wu, T.; He, Y. Synthesis and characterization of a ZrO₂/g-C₃N₄ composite with enhanced visible-light photoactivity for rhodamine degradation. *RSC Adv.* **2014**, *4*, 40029–40035. [[CrossRef](#)]
68. Chen, S.; Hu, Y.; Meng, S.; Fu, X. Study on the separation mechanisms of photogenerated electrons and holes for composite photocatalysts g-C₃N₄-WO₃. *Appl. Catal. B Environ.* **2014**, *150*, 564–573. [[CrossRef](#)]
69. Huang, K.; Hong, Y.; Yan, X.; Huang, C.; Chen, J.; Chen, M.; Shi, W.; Liu, C.J.C. Hydrothermal synthesis of g-C₃N₄/CdWO₄ nanocomposite and enhanced photocatalytic activity for tetracycline degradation under visible light. *CrystEngComm* **2016**, *18*, 6453–6463. [[CrossRef](#)]
70. Dong, F.; Wang, Z.; Sun, Y.; Ho, W.-K.; Zhang, H. Engineering the nanoarchitecture and texture of polymeric carbon nitride semiconductor for enhanced visible light photocatalytic activity. *J. Colloid Interface Sci.* **2013**, *401*, 70–79. [[CrossRef](#)]
71. Yu, Y.; Yan, W.; Wang, X.; Li, P.; Gao, W.; Zou, H.; Wu, S.; Ding, K. Surface engineering for extremely enhanced charge separation and photocatalytic hydrogen evolution on g-C₃N₄. *Adv. Mater.* **2018**, *30*, 1705060. [[CrossRef](#)]

Disclaimer/Publisher’s Note: The statements, opinions and data contained in all publications are solely those of the individual author(s) and contributor(s) and not of MDPI and/or the editor(s). MDPI and/or the editor(s) disclaim responsibility for any injury to people or property resulting from any ideas, methods, instructions or products referred to in the content.